

Cite this: *J. Mater. Chem. C*, 2023,  
11, 2721

# Charge transfer in the Ag–polymer–fullerene system of organic solar cells (OSCs) observed by surface-enhanced Raman spectroscopy: donor/acceptor concentration-dependent†

Daxin Zhang,<sup>abc</sup> Shuo Yang,<sup>d</sup> Wenshi Zhao,<sup>abc</sup> Lili Yang,<sup>id</sup><sup>c</sup> Maobin Wei,<sup>c</sup>  
Lei Chen<sup>id</sup><sup>\*c</sup> and Jinghai Yang<sup>id</sup><sup>\*c</sup>

Currently, modulating the charge transfer (CT) process poses a major challenge for many organic solar cells (OSCs) and monitoring the CT dynamics demands further research. The surface-enhanced Raman spectroscopy (SERS) technique was successfully used herein to monitor the CT process, which was strongly dependent on the carrier density in the Ag–polymer–fullerene system. However, the carrier density can be controlled by the acceptor and donor concentrations. As the acceptor and donor concentrations were changed, significant frequency shifts in the SERS peaks were observed. The donor and acceptor concentration changes exhibited the opposite effects on the frequency shift due to donor-to-acceptor and acceptor-to-donor CT. In addition, the peak intensity at 1450 cm<sup>-1</sup> increased significantly owing to the CT contribution. Thus, the CT process induced the Raman frequency shift and monitoring the peak intensity increase can elucidate the interaction mechanism between the acceptor and donor in OSCs. This study provides a novel insight into the theoretical foundation of CT dynamics in metal–polymer–fullerene systems.

Received 14th December 2022,  
Accepted 26th January 2023

DOI: 10.1039/d2tc05323c

rsc.li/materials-c

## 1 Introduction

Since their discovery in 1995, organic photovoltaic solar cells (OPVs) have gained worldwide interest as a source of renewable energy.<sup>1–3</sup> In particular, organic solar cells (OSCs) are attractive owing to their advantages including thin-film architecture, low material consumption of abundant organic materials, efficient solution processes, and low manufacturing energy requirements,<sup>2–5</sup> opening up new possibilities for applications in agriculture, construction, wearable electronics, and health sciences.<sup>6</sup> A major breakthrough in OSCs technology was the adoption of C<sub>60</sub> derivatives (including [6,6]-phenyl-C61-butyric acid methyl ester fullerene and its derivative, PCBM).<sup>7,8</sup> As a soluble, processable, and stable polymer, poly(3-hexylthiophene) (P3HT) has been used to improve the synthetic feasibility, and chemical and physical

properties of OSCs.<sup>9</sup> Blends of P3HT as the electron donor and PCBM as the electron acceptor are popular polymer–fullerene systems.<sup>10</sup> It is well reported in the literature that the charge transfer (CT) processes are difficult to monitor in the polymer–fullerene system. An extremely high-efficiency photo-induced CT process of approximately 50–100 fs was observed between a conjugated polymer and fullerene derivatives.<sup>11,12</sup> Therefore, the key to overcoming this challenge is to develop an appropriate CT monitoring technique.

Surface-enhanced Raman scattering (SERS) is an extremely sensitive and practical analytical technology that has widespread applications in numerous fields, including the biological, pharmaceutical, contaminant, and toxin detection industries.<sup>13,14</sup> As an important chemical mechanism (CM) of SERS, CT is of interest to many researchers.<sup>15–17</sup> A recent work on the topic utilized an inorganic metal–semiconductor system as a substrate to explore CT between probe molecules and semiconductors.<sup>18</sup> Compared to the inorganic metal–semiconductor system, the organic-based systems are generally more suited to do CT research because of their high stability, higher selectivity, easy adjustment and renewability.<sup>19,20</sup> Another advantage is that the organic semiconductor structure can be altered by tuning the molecular properties, allowing for the customization and optimization of CT.<sup>21</sup> For example, Yilmaz and colleagues adjusted the number of thiophene rings in the central chain of  $\alpha,\omega$ -diperfluorohexylquaterthiophene

<sup>a</sup> Changchun Institute of Optics, Fine Mechanics and Physics, Chinese Academy of Sciences, Changchun 130033, P. R. China

<sup>b</sup> University of Chinese Academy of Sciences, Beijing 100049, P. R. China

<sup>c</sup> Key Laboratory of Functional Materials Physics and Chemistry (Ministry of Education), College of Physics, Jilin Normal University, Changchun 130103, China. E-mail: chenlei@jlnu.edu.cn, jhyang1@jlnu.edu.cn

<sup>d</sup> College of Science, Changchun University, Changchun 130022, P. R. China

† Electronic supplementary information (ESI) available: Experimental, basic characterization of the Ag–fullerene–polymer system and carrier density characterization. See DOI: <https://doi.org/10.1039/d2tc05323c>

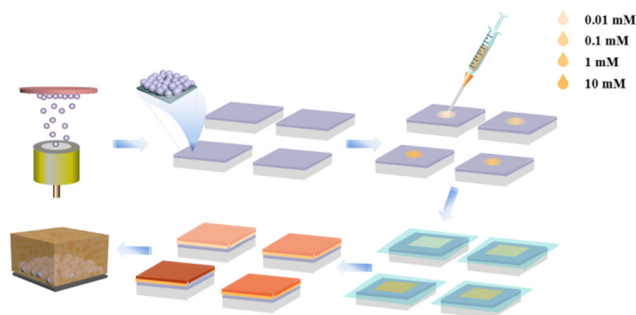
(DFH-4T) (for instance, to DFH-5T), and, in a separate attempt, substituted fluorine atoms with hydrogen (including in  $\alpha,\omega$ -dihexylquaterthiophene (DH-4T)), thus demonstrating precise control over the CT transition locations.<sup>22</sup> However, this experiment is too complicated for practical purposes and a simplified method is needed to study CT. The synergistic effects of surface plasmon resonance (SPR) and CT were analyzed by adjusting the inorganic semiconductor carrier densities. The carrier density can regulate CT to achieve selective CT enhancement in organic semiconductors,<sup>22</sup> similar to that in inorganic semiconductors. Carriers can be classified into donors and acceptors based on their electronegativity, and the effects of donor and acceptor concentration on CT may differ. The regulation of CT by donor and acceptor concentration is largely unexplored in polymer-fullerene systems. SPR can increase active layer (AL) absorbance and scattering without destroying the exciton's diffusion length,<sup>23,24</sup> thus enhancing the CT. In addition, metallic nanoparticles (NPs) can improve the CT and induce morphology changes in the optoelectronic materials.<sup>25</sup> Under high-efficiency CT and SPR, Ag-polymer-fullerene systems have demonstrated good SERS performance, facilitating CT analysis.

Inspired by the above-mentioned literature studies, an Ag-polymer-fullerene system was designed to investigate the CT dependence on carrier density based on SERS. A validated donor/acceptor concentration method was established to control the carrier density. The ultraviolet-visible (UV-vis) absorbance spectra and SERS characterization demonstrated that CT causes a frequency shift and increased SERS intensity in the metal-organic system. These findings are significant for the elucidation of the CT mechanism and monitoring the CT dynamics in OSCs. These results will help us to determine the CT of metals, fullerene derivatives and organic polymer materials by SERS during the device optimization, and evaluate the interaction between organic photoelectric materials, which has a guiding significance for the manufacture of electronic devices.

## 2. Results and discussion

### 2.1 Basic characterization of the Ag-polymer-fullerene system

The Ag-polymer-fullerene system was composed of an Ag NPs thin film prepared by magnetron sputtering using polymer-fullerene ALs *via* one-step growth.<sup>26</sup> A flowchart of the Ag-polymer-fullerene preparation method is illustrated in Scheme 1. Ag/P3HT/PCBM



Scheme 1 A step diagram of the generation method of the films.

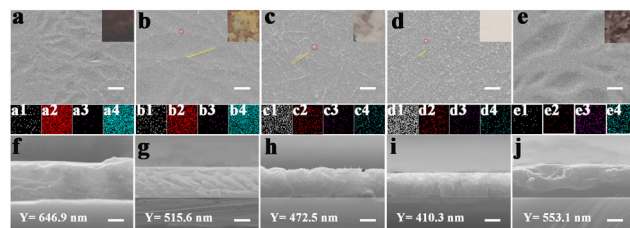


Fig. 1 (a)–(e) The scanning electron microscopy (SEM) of the Ag/P3HT (0.01 mM)/PCBM (10–0.01 mM) (P3HT, PCBM = 1, v/v) (a)–(d), and the Ag/P3HT (0.1 mM) (e). The insets are optical photographs of the corresponding samples. The small red circles represent Ag nanoparticles and the small yellow lines represent nanostructures. (a1)–(e4) The EDS mapping of the elemental distributions, silver (Ag) (white color), oxygen (O) (red color), sulfur (S) (pink color) and carbon (C) (cyan color). (f)–(j) The cross section SEM of the Ag/P3HT (0.01 mM)/PCBM (10–0.01 mM) (P3HT, PCBM = 1, v/v) (f)–(i), and the Ag/P3HT (0.1 mM) (j), corresponding to the SEM. The Y is the thickness of the samples, which is  $\pm 0.1$  nm. The scale bars correspond to 250 nm.

heterostructures with PCBM concentrations ranging from 10 to 0.01 mM were synthesized, and their basic surface morphology was examined by energy dispersive spectrometry (EDS) mapping and scanning electron microscopy (SEM; Fig. 1). From the EDS results, it can be observed that the detected S in P3HT gradually increased (Fig. 1(b1)–(e4)), while O and C decreased, confirming a decreased PCBM concentration. Some nanostructures were observed on the film surface due to the low evaporation rate during growth.<sup>27,28</sup> The Ag/P3HT (0.1 mM) film exhibited stronger and more abundant nanostructures, but with increasing number of nanostructures, their length shortened from  $\sim 470$  to 150 nm with decreasing PCBM concentration from 10 to 0.01 mM. These results indicate that reduced aggregation of P3HT and PCBM prevented crystallization. In addition, the connection between film thickness and PCBM concentration was noted. The Ag/P3HT (0.1 mM) film thickness was approximately 553.1 nm, while that of the Ag/P3HT/PCBM (10–0.01 mM) films decreased from 646.9 to 410.3 nm. To examine the surface morphology, optical photographs of the Ag/P3HT/PCBM (10–0.01 mM) films were taken and they displayed significant color changes (Fig. 1(a)–(e)). These results show that the Ag/P3HT/PCBM (0.1 mM) film is more homogeneous, as verified by the three-dimensional (3D) atomic force microscopy (AFM) image (Fig. 2(a)). The evident nanostructures agree with the SEM images, and the root means square (RMS) surface roughness was determined to be  $\sim 1.4$  nm.<sup>28</sup> The RMS value indicates that the Ag/P3HT/PCBM (0.1 mM) film exhibited a smoother surface between the donor and acceptor.

Relative crystallinity depends on internal morphology changes and has a major contribution to the CT efficiency in photovoltaic devices.<sup>29,30</sup> Therefore, to confirm the crystallinity variation, the structural properties of pure P3HT (powder), pure PCBM (powder), Ag/P3HT, Ag/PCBM, and Ag/P3HT/PCBM thin films on Si wafers were further characterized by X-ray diffraction (XRD, Fig. 2(b) and (c)). Pure PCBM powder exhibited a distinct diffraction pattern with characteristic narrow peaks of a microcrystalline structure without diffraction signal contributions. Thus, the diffraction peak of Ag (111) at  $2\theta = 38^\circ$  was observed

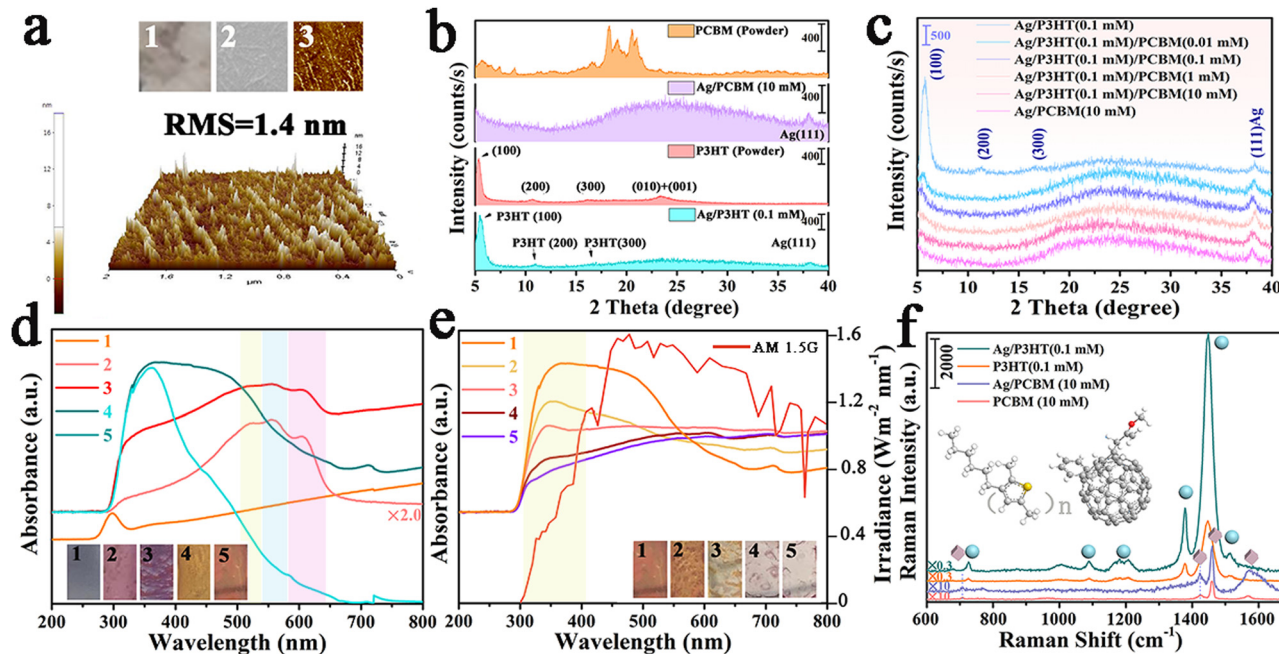


Fig. 2 (a) The three-dimensional (3D) height sensor AFM image of Ag/P3HT/PCBM (0.1 mM), and the root mean square (RMS) surface roughness is  $\sim 1.4$  nm. The illustrations show the optical photographs (1), SEM (2), and surface topography (3) of Ag/P3HT/PCBM (0.1 mM). (b) XRD pattern of PCBM (powder), Ag/PCBM (10 mM), P3HT (powder), and Ag/P3HT (0.1 mM) films (cast from chloroform solutions by air evaporation). (c) XRD pattern of the thin films. (d) UV-vis absorbance spectra of the thin films, (1) Ag, (2) P3HT (0.01 mM), (3) Ag/P3HT (0.01 mM), (4) PCBM (10 mM) and (5) Ag/PCBM (10 mM). The illustrations show the optical photographs of these samples. (e) UV-vis absorbance spectra of the thin films, Ag/PCBM (10 mM) (1), Ag/P3HT (0.01 mM)/PCBM (10–0.01 mM) (2–5), and solar spectrum at AM 1.5G. (f) Normalized Raman spectra of the samples. The illustration shows the structural formula of the P3HT and PCBM. Acquisition time, 30 s. Accumulations, 2. Laser power, 20 mW. Excitation laser, 514.5 nm.

only for the Ag/PCBM thin film.<sup>31,32</sup> Compared to PCBM, many diffraction peaks were observed in the P3HT powder, with a prominent diffraction peak at  $2\theta = 5.3^\circ$  attributed to the primary (100). This is in accordance with polymer crystallites with an  $a$ -axis orientation (main chain parallel and side chains perpendicular to the substrate). This also corresponds to an interlayer  $d$ -spacing of  $1.61 \pm 0.20$  nm in the well-organized lamellar structure.<sup>16,33</sup> The other diffraction peaks of the P3HT powder at  $2\theta = 10.7$  and  $15.9^\circ$  correspond to the secondary (200) and tertiary (300) peaks assigned to the  $a$ -axis orientation, respectively, and the peak at  $2\theta = \sim 23^\circ$  corresponds to the (010) and (001) peaks arising from  $\pi$ - $\pi^*$  interchain stacking.<sup>33,34</sup> Although the P3HT (010) and (001) peaks were absent owing to the  $\pi$ - $\pi^*$  interchain stacking destruction, the P3HT (100) and Ag (111) peaks were observed in the Ag/P3HT film. The P3HT (100) peak intensity is proportional to the number of P3HT nano-domains per unit volume and is indicative of the thin film crystallinity.<sup>8</sup> The Ag/P3HT crystallinity was higher than that of P3HT, as confirmed by the higher Ag/P3HT (100) peak. The decreasing (100) peak height suggests that the Ag/P3HT/PCBM crystallinity decreased due to the presence of PCBM molecules disrupting P3HT crystallinity.<sup>35</sup> In addition, the Ag/P3HT/PCBM film crystallinity gradually decreased due to the aggregation of P3HT and PCBM.<sup>36,37</sup> These results indicate that PCBM addition forms a network interpenetration structure with P3HT at the interface, but excess PCBM can aggregate with P3HT and decrease the overall crystallinity,<sup>38</sup> impeding carrier extraction

and CT. Although the crystallinity changed, the height and diffraction of the Ag(111) peaks remained constant. Herein, the Ag substrate was not involved with the initial crystallization of the P3HT chains and subsequent aggregation of PCBM during the morphology evolution process of the Ag/P3HT/PCBM films.<sup>37</sup> However, the SPR effect of Ag may enhance UV absorbance and Raman scattering, which would be conducive to CT in the Ag/P3HT/PCBM films.<sup>39</sup>

Another factor that is relevant for OSCs photoelectric conversion is the light absorbance capability that can be investigated using UV-vis absorbance spectra (Fig. 2(d) and (f)). The Ag thin film expanded the light absorption into the deep UV region, allowing high energy to be used for photoelectric conversion. The P3HT absorbance peaks were observed in the visible region at  $\sim 600$ , 550, and 515 nm, as observed in the Ag/P3HT (0.01 mM) film.<sup>40,41</sup> The absorbance peaks at  $\sim 515$  and 550 nm were ascribed to the P3HT (010) and (001) peaks, arising from the intrinsic  $\pi \rightarrow \pi^*$  (the 0–0 and 0–1) transitions of P3HT. The obvious shoulder centralized at  $\sim 615$  nm indicates a highly interchain-delocalized excitation and high P3HT crystallinity.<sup>35,42</sup> Meanwhile, the higher energy transition of P3HT at  $\sim 300$  nm is related to electron and phonon transitions.<sup>43</sup> The donor polymer P3HT showed a strong light absorbance in the visible region, whereas the fullerene-based PCBM acceptor mainly absorbs light in the near UV region. The dominant electron transitions in C<sub>60</sub> and its tail extended to the near-infrared region due to light scattering or other experimental artifacts.<sup>37</sup> Compared with the P3HT and PCBM films, the peak

intensity of the Ag/P3HT and Ag/PCBM films dramatically increased in the 300–600 nm region due to the SPR effect of Ag. The Ag/P3HT/PCBM films showed a strong absorbance in line with the Ag/P3HT and Ag/PCBM films, as indicated by the simple superposition of the two materials (Fig. 2(e)).<sup>40</sup> The Ag/P3HT/PCBM films exhibited broader absorbance and the absorbance peak at  $\sim 300$  nm showed a small blueshift, reflecting weak intermolecular interactions and molecular aggregation with decreasing PCBM concentration.<sup>44</sup> Additionally, interchain interaction can slightly impact Raman scattering. This UV-vis absorbance spectra analysis suggests a suitable PCBM concentration range for acceptable light capture ability to absorb more solar radiation, accelerate exciton dissociation, and achieve high efficiency CT in OSCs.

The CT between donor and acceptor in OSCs is complex and occurs in approximately 50–100 fs, complicating its experimental determination. To further understand the CT mechanisms in Ag/P3HT/PCBM films, SERS was used to monitor CT between the donor and acceptor. SERS at 514.5 nm excitation is shown in Fig. 2(f) for the PCBM (10 mM), Ag/PCBM (10 mM), P3HT (0.1 mM), and Ag/P3HT (0.1 mM) thin films, along with the chemical structure of P3HT and PCBM.<sup>47</sup> The observed frequency shifts and SERS peak assignments are summarized in Table S1 (ESI<sup>†</sup>).<sup>10,46–48</sup> The strong resonance Raman peaks of P3HT were obtained based on the 514.5 nm laser excitation because of the absorbance peak at  $\sim 500$  nm. The predominant peaks are located at  $\sim 1450$  and  $1380$   $\text{cm}^{-1}$ , which were assigned to the  $\text{C}_\alpha=\text{C}_\beta$

symmetric stretching mode and  $\text{C}_\beta-\text{C}_\beta$  skeletal stretching mode, respectively. The weak peaks at  $\sim 724.6$ , 1003.0, 1088.4, 1169.1, 1184.8, 1205.2, and 1514.2  $\text{cm}^{-1}$  were ascribed to the antisymmetric ring  $\text{C}_\alpha-\text{S}-\text{C}_\alpha$  stretching,  $\text{C}_\beta-\text{C}_{\text{alkyl}}$  stretching, C–H bending, symmetric  $\text{C}_\alpha-\text{C}_\alpha$  stretching, and a combination of  $\text{C}_\alpha-\text{C}_\alpha$  stretching,  $\text{C}_\beta-\text{H}$  stretching, and  $\text{C}_\alpha=\text{C}_\beta$  antisymmetric stretching modes, respectively.<sup>45</sup> In the Raman spectra of the as-prepared pristine PCBM thin film, the dominant pentagonal-pinch mode Ag(2) of the  $\text{C}_{60}$  molecule was observed at  $\sim 1460.7$   $\text{cm}^{-1}$ , with three weak peaks at  $\sim 709.1$ , 1425.0 and 1573.6  $\text{cm}^{-1}$  arising from the Hg(3), Hg(7), and Hg(8) Raman modes of the  $\text{C}_{60}$  molecule, respectively.<sup>48</sup> The observed frequency shifts and SERS peak assignments of Ag/P3HT and Ag/PCBM were the same as those of P3HT and PCBM, but the SERS intensities of the Ag/P3HT and Ag/PCBM films were significantly stronger than those of P3HT and PCBM due to the SPR effect of Ag. For the Ag/P3HT/PCBM and Ag/PCBM/P3HT systems, the peak at 1450  $\text{cm}^{-1}$  was fitted and assigned to the  $\text{C}_\alpha=\text{C}_\beta$  symmetric stretch mode and pentagonal-pinch mode Ag(2) of the  $\text{C}_{60}$  molecule, respectively. The other SERS peaks arose from the pure P3HT and PCBM and their assignments are summarized in Table S1 (ESI<sup>†</sup>). The SERS behavior can be altered by CT between the donor and acceptor in the polymer–fullerene system OSCs. The donor and acceptor concentration effects on CT are opposite and interfering. Thus, the donor and acceptor concentration-dependent SERS spectra are shown in Fig. 3 and described in detail below. The microscopic CT processes in the OSCs system were also evaluated based on the SERS mechanism.

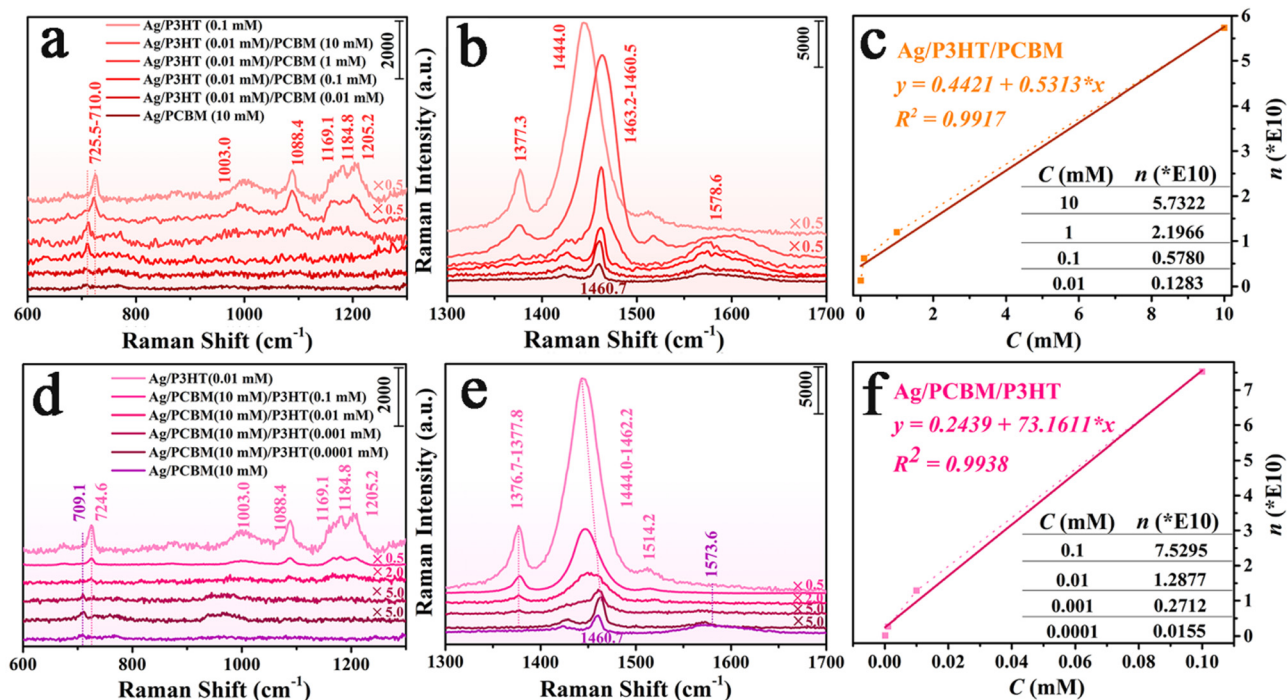


Fig. 3 (a and b) SERS spectra of the Ag/P3HT/PCBM (P3HT, PCBM = 1, v/v), in which the concentration of the P3HT is 0.01 mM, and the concentration of the PCBM is 10  $\sim$  0.01 mM, respectively. (c) The fitting curves of carrier density ( $n$ ) and concentration ( $C$ ) in the Ag/P3HT/PCBM system. (d and e) SERS spectra of the Ag/PCBM/P3HT (=1, v/v), in which the concentration of the PCBM is 10 mM, and the concentration of the P3HT is 0.1–0.0001 mM, respectively. Acquisition time, 30 s. Accumulations, 2. Laser power, 20 mW. Excitation laser, 514.5 nm. (f) The fitting curves of carrier density ( $n$ ) and concentration ( $C$ ) in the Ag/PCBM/P3HT system.

The peaks in these spectra were measured with an accuracy of  $\pm 0.1 \text{ cm}^{-1}$ , as indicated by line-shape analyses of the different peaks.

## 2.2 Acceptor concentration-dependent CT

The effect of acceptor concentrations on CT between the donor and acceptor in the OSCs was investigated by SERS of Ag/P3HT/PCBM (10–0.01 mM) with various acceptor concentrations and the spectra are shown in Fig. 3(a) and (b). Compared to the SERS intensities of the Ag/P3HT system, that of the Ag/P3HT/PCBM system decrease, likely due to weak intermolecular interactions. Nevertheless, with increasing acceptor concentrations, the SERS intensities of the Ag/P3HT/PCBM (10–0.01 mM) system increase due to the electromagnetic field enhancement created by the acceptor magnetic dipole. The SERS intensity at  $\sim 1450 \text{ cm}^{-1}$  notably increases and the peak was blue shifted, demonstrating that CT in the Ag/P3HT/PCBM (10–0.01 mM) enhances the SERS intensities.

Using the definition of the Raman activity, absolute differential Raman cross-section (implicitly for a Stokes process) is expressed in terms of frequency shifts, at a temperature  $T$ , in a medium of refractive index  $n_M$ , as

$$d\sigma_k^{ST}/d\Omega = C b_k^2 L_M R_k \nu_R^4 (1 + n_k^B(T)) \quad (1)$$

And the different contributions are separated in eqn (1).

The SERS intensity is dependent on the Raman cross section, and the SERS intensity of the peak at  $\sim 1450 \text{ cm}^{-1}$  can be expressed as follows:

$$I_{1450} \propto d\sigma_k^{ST}/d\Omega = C b_k^2 L_M R_k \nu_R^4 (1 + n_k^B(T)) \quad (2)$$

Here the CT contribution appears in the form of a frequency shift, referred to as  $\nu_R$ . In eqn (2),  $C$  is a constant, and  $b_k^2$ ,  $L_M$ , and  $R_k$  do not depend on the carrier density, representing the square of the zero-point amplitude of the normal mode in reduced-mass coordinates, the local field correction factor, and Raman activity, respectively. The factor proportional to  $\nu_R^4$  can be approximated to a constant. Thus,  $I_{1450} \propto \nu_R^4$ . It has been documented that Raman intensity is related to carrier density, as obtained by the Hall element in Table S2 (ESI<sup>†</sup>). According to the fitting of SERS peak intensity at  $1450 \text{ cm}^{-1}$  with carrier density ( $n$ ),  $I_{1450} \propto n$ , a 99% correlation was obtained. Thus, the acceptor concentration ( $C_A$ ) regulates the carrier density, as described by  $I_{1450} \propto \nu_R^4 \propto C$ , and accelerates CT.

For the Ag/P3HT/PCBM system, CT arises from the three pathways shown in Fig. 4(a): (i) a metal-to-molecule CT resonance ( $CT'_{Ag-P3HT}$ ), (ii) a molecule-to-molecule CT from the highest occupied molecular orbital (HOMO) of the PCBM to the HOMO of the P3HT ( $CT'_{PCBM-P3HT}$ ), and (iii) molecule-to-molecule CT from the HOMO of the P3HT to the lowest unoccupied molecular orbital (LUMO) of the PCBM ( $CT'_{P3HT-PCBM}$ ).  $CT'_{Ag-P3HT}$  does not depend on the PCBM concentration, whereas  $CT'_{P3HT-PCBM}$  and  $CT'_{PCBM-P3HT}$  are associated with PCBM concentration. According to the previous analysis, carrier density accelerates CT. Combined with the relationship between the three CT paths and carrier density in the Ag/P3HT/PCBM system,  $CT'_{P3HT-PCBM}$  and

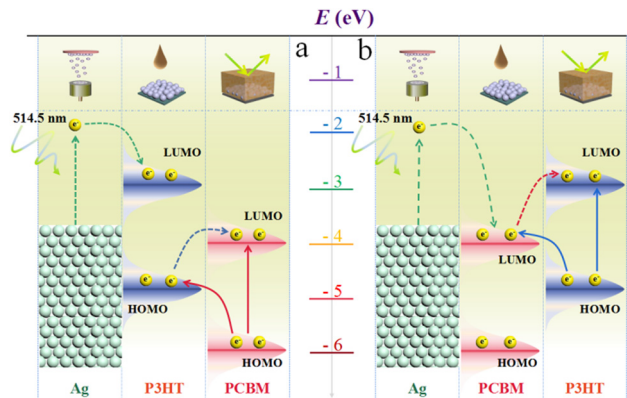


Fig. 4 Energy level and electron transition diagrams of the Ag/P3HT/PCBM (a) and Ag/PCBM/P3HT (b) systems under 514.5 nm excitation, respectively. At the top of (a) and (b) are illustrations of the flowchart of the magnetron sputtering technology and one-step growth method.

$CT'_{PCBM-P3HT}$  could change the SERS intensity and shift at  $\sim 1450 \text{ cm}^{-1}$ . Without considering the coupling contribution,  $I_{1450}$  can be simplified as follows:

$$I_{1450} \propto CT'_{P3HT-PCBM} + CT'_{PCBM-P3HT} \propto C_D \quad (3)$$

To determine two CT contributions to SERS intensity at  $1450 \text{ cm}^{-1}$  with increasing acceptor concentrations, the mixed SERS intensity of  $1450 \text{ cm}^{-1}$  was divided into two peaks at  $1460.7$  and  $1444.0 \text{ cm}^{-1}$  arising from P3HT and PCBM (Fig. 5), respectively, which are affected by  $CT'_{PCBM-P3HT}$  and  $CT'_{P3HT-PCBM}$ , respectively. The fitting and original peaks at  $1460.7$ ,  $1444.0$ , and  $1450 \text{ cm}^{-1}$  are shown in Fig. 5(a) and (b). Moreover, the SERS intensity at  $1440 \text{ cm}^{-1}$  is relatively small, that is, it is a small contribution to SERS intensity in the Ag/P3HT/PCBM system. The fitting mixed peaks were obtained in Fig. 5(a) and (b). The fitting mixed peaks are overlapped with the original mixed peaks in a large amount in Fig. 5(a) and (b), proving that the fitting effect is very good. The line plots of the fitting mixed peak intensity, original mixed peak intensity and carrier density are shown in Fig. 5(c) and (d), and the specific values are also shown in the illustration of Fig. 5(c) and (d). There are also difference values between the fitting mixed and original peak in the illustration, and the difference values are relatively small or even 0. The calculated peak intensity at  $\sim 1450 \text{ cm}^{-1}$  can be expressed as follows:

$$I_{cal} = 0.96 \times I_{1460.7} + 0.04 \times I_{1440.0} \quad (4)$$

Here,  $I_{ori}$ ,  $I_{1460.7}$ , and  $I_{1440.0}$  are the peak intensities at  $\sim 1450$ ,  $1460.7$  and  $1440.0 \text{ cm}^{-1}$ , respectively.  $I_{cal}$  is the calculated peak intensity at  $\sim 1450 \text{ cm}^{-1}$ . A good fitting effect is shown in Fig. 5(c) due to the negligible difference value between the  $I_{cal}$  and  $I_{ori}$ . Based on eqn (4), the  $I_{1460.7}$  value of PCBM contributes more to  $I_{1450}$  owing to its larger multiple than the  $I_{1440.0}$  value of P3HT. Therefore,  $I_{1450} \propto CT'_{PCBM-P3HT} \propto C_A$ , indicating that the increasing acceptor concentration promotes exciton separation at the acceptor interface, hindering their recombination, and increasing their lifetime and diffusion length, thereby

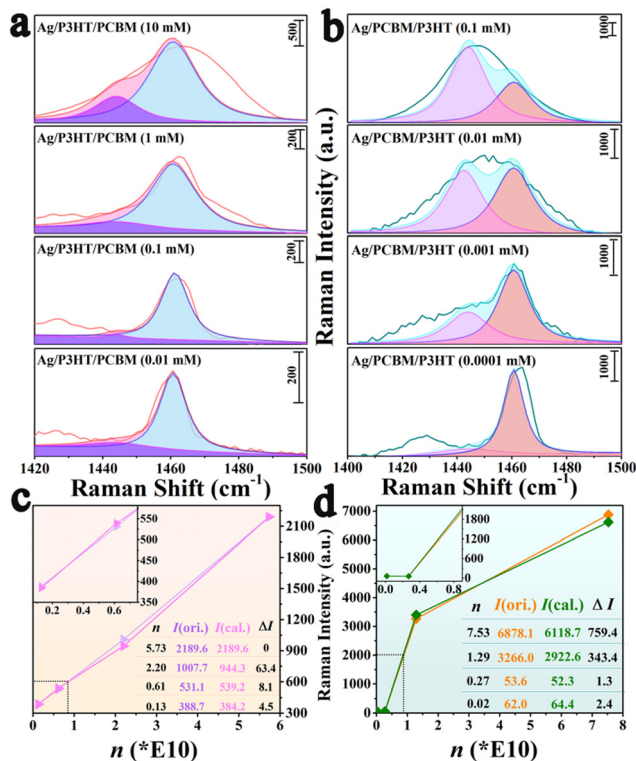


Fig. 5 (a and b) The SERS intensities of Ag/P3HT/PCBM (10–0.01 mM) and Ag/PCBM/P3HT (0.1–0.0001 mM) at  $\sim 1450 \text{ cm}^{-1}$  are divided into  $\sim 1444.0$  and  $1460.7 \text{ cm}^{-1}$ . (c and d) The line chart of the Raman intensities of Ag/P3HT/PCBM (10–0.01 mM) (c) and Ag/PCBM/P3HT (0.1–0.0001 mM) (d) and concentration of the PCBM. (The pink and green lines represent the calculated Raman intensity of Ag/P3HT/PCBM (10–0.01 mM) and Ag/PCBM/P3HT (0.1–0.0001 mM), the purple and yellow lines represent the original Raman intensity of Ag/P3HT/PCBM (10–0.01 mM) and Ag/PCBM/P3HT (0.1–0.0001 mM)). The inset illustrations show the numerical value of the original Raman intensity ( $I_{\text{ori}}$ ), calculated Raman intensity ( $I_{\text{cal}}$ ) and difference value between the original Raman intensity and calculated Raman intensity ( $\Delta I$ ).

improving the CT efficiency. This result also demonstrates that the acceptor concentrations can specifically enhance the CT from the HOMO of the acceptor to the HOMO of the donor in the polymer–fullerene system, thus increasing the photoelectric conversion efficiency and improving the device OSCs performance.

### 2.3 Donor concentration-dependent CT

Compared to the acceptor concentrations, a different concentration-dependent SERS of the donor was observed (Fig. 3(c) and (d)). Thus, the effect of donor concentrations on the CT between donor and acceptor was further investigated. The SERS intensities of the Ag/PCBM/P3HT (0.1–0.0001 mM) increased with increasing donor concentrations due to EM contributions and the peak at  $\sim 1450 \text{ cm}^{-1}$  significantly increased, similar to the acceptor concentration-dependent SERS. In contrast, the  $\sim 1450 \text{ cm}^{-1}$  peak shifted to a lower frequency due to CT, as described in eqn (2),  $I_{1450} \propto \nu_{\text{R}}^4 \propto \text{CT}$ . Accordingly, the SERS intensity was fitted at  $1450 \text{ cm}^{-1}$  with the carrier density,  $I_{1450} \propto n$ . The donor concentration ( $C_{\text{D}}$ ) regulates the carrier density,  $I_{1450} \propto \text{CT} \propto C_{\text{D}}$ . For the Ag/PCBM/P3HT system, CT arises from the

following three pathways (Fig. 4(b)): (i) metal-to-molecule CT resonances ( $\text{CT}_{\text{Ag-PCBM}}$ ), (ii) molecule-to-molecule CT from the HOMO of P3HT to the LUMO of PCBM ( $\text{CT}_{\text{P3HT-PCBM}}''$ ), and (iii) molecule-to-molecule CT from the LUMO of PCBM to the LUMO of P3HT ( $\text{CT}_{\text{PCBM-P3HT}}''$ ).  $\text{CT}_{\text{Ag-PCBM}}$  does not depend on the PCBM concentration. Therefore, without considering the coupling contribution, the following expression can be obtained:

$$I_{1450} \propto \text{CT}_{\text{P3HT-PCBM}}'' + \text{CT}_{\text{PCBM-P3HT}}'' \propto C_{\text{A}} \quad (5)$$

Furthermore, the contribution of  $\text{CT}_{\text{PCBM-P3HT}}''$  and  $\text{CT}_{\text{P3HT-PCBM}}''$  to the SERS intensity at  $1450 \text{ cm}^{-1}$  with increasing donor concentrations allows the SERS peak at  $1450 \text{ cm}^{-1}$  in the Ag/PCBM/P3HT system to be expressed as follows:

$$I_{\text{cal}} = 1.2 \times I_{1444.0} - 0.2 \times I_{1460.7} \quad (6)$$

$I_{1444.0}$  and  $I_{1460.7}$  are affected by  $\text{CT}_{\text{P3HT-PCBM}}''$  and  $\text{CT}_{\text{PCBM-P3HT}}''$ , respectively, and an acceptable fit was obtained with negligible difference between the  $I_{\text{cal}}$  and  $I_{\text{ori}}$ . According to eqn (6),  $I_{1444.0}$  of P3HT contributes more strongly due to its larger coefficient than the  $I_{1460.7}$  of PCBM, proving  $I_{1450} \propto \nu_{\text{R}}^4 \propto \text{CT}_{\text{P3HT-PCBM}}'' \propto C_{\text{D}}$ . Therefore,  $\text{CT}_{\text{P3HT-PCBM}}''$  causes the SERS intensity increase and red frequency shift with increasing donor concentration. Furthermore, the donor concentrations mainly induce CT from the HOMO of the donor to the HOMO of the acceptor in the OSCs polymer–fullerene system. From the above discussion, it can be concluded that although the donor and acceptor concentrations can both enhance light capture ability and promote exciton dissociation, the donor and acceptor concentration effects on CT differ as expected. In this study, it was demonstrated that the donor and acceptor concentrations can be used to precisely tune the CT enhancement. Thus, the CT orientation in the polymer–fullerene system of OSCs can be finely controlled by tuning the donor and acceptor concentrations and monitored by SERS.

## 3. Conclusions

In summary, CT dynamics were studied in a metal–donor–acceptor system, adopting a classic polymer–fullerene OSCs system as a representative donor–acceptor system with Ag SPR effects. Moreover, SERS technology was successfully applied to monitor the CT dynamics that were dependent on the donor/acceptor concentrations in the metal–polymer–fullerene system. There are two SERS performances with increasing donor/acceptor concentrations, one is SERS intensity owing to the CT and EM, the other is SERS frequency shifts. Different frequency shifts were observed depending on the underlying CT mechanism. Donor concentrations mainly induce CT from the HOMO of the donor to the LUMO of the acceptor; however, the acceptor concentrations can specifically enhance the CT from the HOMO of the acceptor to the HOMO of the donor. These results also demonstrate that SERS technology was able to accurately monitor the microscopic CT dynamics in the metal–polymer–fullerene system and modulation of the donor/acceptor concentrations is an effective strategy for tuning the CT between organic photoelectric

materials. The tuning highlights potential characteristics that can be exploited by the OSCs for developing high-performance organic photoelectric materials, achieving high PCE of OSCs.

## Author contributions

Zhang D and Zhao W designed the samples and performed the experiments; Yang J and Yang L acquired funding and administered the project; Zhang D and Chen L performed the data analysis; Zhang D wrote the paper with support from Chen L; Yang S and Wei M contributed to the theoretical analysis. All authors contributed to the general discussion.

## Conflicts of interest

There are no conflicts to declare.

## Acknowledgements

This work was supported by the National Natural Science Foundation of China (Grant no. 22075101), the Program for the Development of Science and Technology of Jilin province (Item no. 20200801032GH), the Program of Jilin Provincial Development and Reform Commission (grant no. 2021C036-3), and the Thirteenth Five-Year Program for Science and Technology of Education Department of Jilin Province (grant no. JJKH20210611KJ, JJKH20220432KJ).

## Notes and references

- G. Yu, J. Gao, J. C. Hummelen, F. Wudl and A. J. Heeger, *Science*, 1995, **270**, 1789–1791.
- G. Li, R. Zhu and Y. Yang, *Nat. Photonics*, 2012, **6**, 153–161.
- C. Yan, J. Qin, Y. Wang, G. Li and P. Cheng, *Adv. Energy Mater.*, 2022, **12**, 2201087.
- V. Nair, A. Kumar, C. Subramaniam, P. Malhotra, K. Khandelwal, S. Biswas, F.-C. Chen and G. D. Sharma, *J. Mater. Chem. C*, 2022, **10**, 17781–17811.
- M. Kaltenbrunner, M. S. White, E. D. Glowacki, T. Sekitani, T. Someya, N. S. Sariciftci and S. Bauer, *Nat. Commun.*, 2012, **3**, 1–7.
- Y. Hu, J. Wang, C. Yan and P. Cheng, *Nat. Rev. Mater.*, 2022, **7**, 836–838.
- M. T. Dang, L. Hirsch and G. Wantz, *Adv. Mater.*, 2011, **23**, 3597–3602.
- M. Morana, M. Wegscheider, A. Bonanni, N. Kopidakis, S. Shaheen, M. Scharber, Z. Zhu, D. Waller, R. Gaudiana and C. Brabec, *Adv. Funct. Mater.*, 2008, **18**, 1757–1766.
- T.-A. Chen, X. Wu and R. D. Rieke, *J. Am. Chem. Soc.*, 1995, **117**, 233.
- S. Wang, C. Yang, X. Li, H. Jia, S. Liu, X. Liu, T. Minari and Q. Sun, *J. Mater. Chem. C*, 2022, **10**, 6196–6221.
- H. Kaçuş, Ş. Aydoğan, M. Biber, Ö. Metin and M. Sevim, *Mater. Res. Express*, 2019, **6**, 095104.
- Y. Kim, S. A. Choulis, J. Nelson, D. D. C. Bradley, S. Cook and J. R. Durrant, *Appl. Phys. Lett.*, 2005, **86**, 063502.
- J. F. Li, Y. F. Huang, Y. Ding, Z. L. Yang, S. B. Li, X. S. Zhou, F. R. Fan, W. Zhang, Z. Y. Zhou, D. Y. Wu, B. Ren, Z. L. Wang and Z. Q. Tian, *Nature*, 2010, **464**, 392–395.
- J. Langer, D. J. de Aberasturi, J. Aizpurua, R. A. Alvarez-Puebla, B. Auguie, J. J. Baumberg, G. C. Bazan, S. E. J. Bell, S. E. J. Boisen, A. G. Brolo, J. Choo, D. Ciialla-May, V. Deckert, L. Fabris, K. Faulds, F. J. G. de Abajo, R. Goodacre, D. Graham, A. J. Haes, C. L. Haynes, C. Huck, T. Itoh, M. Ka, J. Kneipp, N. A. Kotov, H. Kuang, E. C. Le Ru, H. K. Lee, J. F. Li, X. Y. Ling, S. A. Maier, T. Mayerhofer, M. Moskovits, K. Murakoshi, J. M. Nam, S. Nie, Y. Ozaki, I. Pastoriza-Santos, J. Perez-Juste, J. Popp, A. Pucci, S. Reich, B. Ren, G. C. Schatz, T. Shegai, S. Schlucker, L. L. Tay, K. G. Thomas, Z. Q. Tian, R. P. Van Duyne, T. Vo-Dinh, Y. Wang, K. A. Willets, C. Xu, H. Xu, Y. Xu, Y. S. Yamamoto, B. Zhao and L. M. Liz-Marzan, *ACS Nano*, 2020, **14**, 28–117.
- H. Liu, Y. Guo, Y. Wang, H. Zhang, X. Ma, S. Wen, J. Jin, W. Song, B. Zhao and Y. Ozaki, *J. Hazard. Mater.*, 2021, **405**, 124642.
- P. L. Stiles, J. A. Dieringer, N. C. Shah and R. P. Van Duyne, *Annu. Rev. Anal. Chem.*, 2008, **1**, 601–626.
- W. Ji, L. Li, W. Song, X. Wang, B. Zhao and Y. Ozaki, *Angew. Chem., Int. Ed.*, 2019, **58**, 14452–14456.
- X. X. Han, W. Ji, B. Zhao and Y. Ozaki, *Nanoscale*, 2017, **9**, 4847–4861.
- J. R. Lombardi, *Nat. Mater.*, 2017, **16**, 878–880.
- S. Guo, Y. Hu, M. Qin, J. Li, Y. Wang, J. Qin and P. Cheng, *Mater. Horiz.*, 2022, **9**, 2097–2108.
- M. Yilmaz, E. Babur, M. Ozdemir, R. L. Giesecking, Y. Dede, U. G. C. Schatz, A. Facchetti, H. Usta and G. Demirel, *Nat. Mater.*, 2017, **16**, 918–924.
- B. Han, L. Chen, S. Jin, S. Guo, J. Park, H. S. Yoo, J. H. Park, B. Zhao and Y. M. Jung, *J. Phys. Chem. Lett.*, 2012, **12**, 7612–7618.
- Y. Z. Yang, L. Sun, J. M. Ou, Y. T. He, X. F. Lin, Z. K. Yuan, W. S. Lin, W. Hong, D. S. Yu, X. D. Chen and Z. R. Qiu, *J. Raman Spectrosc.*, 2016, **47**, 888–894.
- C. H. Kim, S. H. Cha, S. C. Kim, M. Song, J. Lee, W. S. Shin, S. J. Moon, J. H. Bahng, N. A. Kotov and S. H. Jin, *ACS Nano*, 2011, **5**, 3319–3325.
- D. Zhang, S. Yang, X.-Y. Zhang, N. Ma, B. Han, W. Zhao, S. Chi, Y. Liu, J. Yang and L. Chen, *Spectrochim. Acta, Part A*, 2020, **238**, 118430.
- J. Xing, Y. Zou, C. Zhao, Z. Yu, Y. Shan, W. Kong, X. Zheng, X. Li, W. Yu and C. Guo, *Mater. Today Phys.*, 2020, **14**, 7.
- H. L. Huang, G. B. Yi, X. H. Zu, B. B. Zhong and H. S. Luo, *J. Polym. Sci.*, 2017, **35**, 623–630.
- A. Knoll, A. Horvat, K. S. Lyakhova, G. Krausch, G. J. A. Sevink, A. V. Zvelindovsky and R. Magerle, *Phys. Rev. Lett.*, 2002, **89**, 05501.
- L. Zhu, P. Li, H. Sun, X. Han, Y. Xua, X. Wang, B. Liu, Y. Ozaki and B. Zhao, *J. Mater. Chem. C*, 2021, **9**, 2660–2684Z.
- Z. Wang, M. Das, C. Gutheil, H. Osthues, F. Strieth-Kalthoff, A. Timmer, N. L. Doltsinis, W. Wang, L. Chi and F. Glorius, *J. Mater. Chem. C*, 2022, **10**, 8589–8595.
- T. Erb, U. Zhokhavets, G. Gobsch, S. Raleva, B. Stühn, P. Schilinsky, C. Wadauf and C. J. Brabec, *Adv. Funct. Mater.*, 2005, **15**, 1193–1196.

- 32 X. Yang, J. K. J. van Duren, M. T. Rispens, J. C. Hummelen, R. A. J. Janssen, M. A. J. Michels and J. Loos, *Adv. Mater.*, 2004, **16**, 802–806.
- 33 Y. Kim, S. Cook, S. M. Tuladhar, S. A. Choulis, J. Nelson, J. R. Durrant, D. D. C. Bradley, M. Giles, I. McCulloch, C. S. Ha and M. Ree, *Nat. Mater.*, 2006, **5**, 197–203.
- 34 Y. K. Jung and F. C. Daniel, *J. Phys. Chem. C*, 2008, **112**, 17726–17736.
- 35 M. Campoy-Quiles, T. Ferenczi, T. Agostinelli, P. G. Etchegoin, Y. Kim, T. D. Anthopoulos, P. N. Stavrinou, D. D. C. Bradley and J. J. Nelson, *Nat. Mater.*, 2008, **7**, 158–164.
- 36 J. Gao, A. K. Thomas, R. Johnson, H. Guo and J. K. Grey, *Chem. Mater.*, 2004, **26**, 4395–4404.
- 37 J. Clark, C. Silva, R. H. Friend and F. C. Spano, *Phys. Rev. Lett.*, 2007, **98**, 206406.
- 38 X. N. Yang, J. Loos, S. C. Veenstra, W. J. H. Verhees, M. M. Wienk, J. M. Kroon, M. A. J. Michels and R. A. J. Janssen, *Nano Lett.*, 2005, **5**, 579–583.
- 39 Samriti, V. Rajput, R. K. Gupta and J. Prakash, *J. Mater. Chem. C*, 2022, **10**, 73–95.
- 40 B. Jarzabek, P. Nitschke, B. Hajduk, M. Domanski and H. Bednarski, *Polym. Test.*, 2020, **88**, 106573.
- 41 T.-F. Guo, T.-C. Wen, G. L'Vovich Pakhomov, X.-G. Chin, S.-H. Liou, P.-H. Yeh and C.-H. Yang, *Thin Solid Films*, 2018, **516**, 3138–3142.
- 42 R. Osterbacka, C. P. An, X. M. Jiang and Z. V. Vardeny, *Science*, 2000, **287**, 839–842.
- 43 F. C. Wu, Y. C. Huang, H. L. Cheng, W. Y. Chou and F. C. Tang, *J. Phys. Chem. C*, 2011, **115**, 15057–15066.
- 44 J. Clark, J. F. Chang, F. C. Spano, R. H. Friend and C. Silva, *Appl. Phys. Lett.*, 2009, **94**, 3.
- 45 V. Saini, Z. Li, S. Bourdo, E. Dervishi, Y. Xu, X. Ma, V. P. Kunets, G. J. Salamo, T. Viswanathan, A. R. Biris, D. Saini and A. S. Biris, *J. Phys. Chem. C*, 2009, **113**, 8023–8029.
- 46 H. Kuzmany, M. Matus, B. Burger and J. Winter, *Adv. Mater.*, 1994, **6**, 731–745.
- 47 S. Falke, P. Eravuchira, A. Materny and C. Lienau, *J. Raman Spectrosc.*, 2011, **42**, 1897–1900.
- 48 L.-C. Shih, S.-R. Lin, R. Chaurasiya, P.-Y. Kung, S.-S. Jhang, B. H. Liu, Y.-H. Su and J.-S. Chen, *J. Mater. Chem. C*, 2022, **10**, 8181–8191.